

# Silicon heterojunction solar cell with passivated hole selective $\text{MoO}_x$ contact

Corsin Battaglia,<sup>1,2</sup> Silvia Martín de Nicolás,<sup>3</sup> Stefaan De Wolf,<sup>3</sup> Xingtian Yin,<sup>1,2</sup> Maxwell Zheng,<sup>1,2</sup> Christophe Ballif,<sup>3</sup> and Ali Javey<sup>1,2,a)</sup>

<sup>1</sup>Electrical Engineering and Computer Sciences Department, University of California, Berkeley, California 94720, USA

<sup>2</sup>Materials Sciences Division, Lawrence Berkeley National Laboratory, Berkeley, California 94720, USA

<sup>3</sup>Photovoltaics and Thin Film Electronics Laboratory, Ecole Polytechnique Fédérale de Lausanne, 2000 Neuchâtel, Switzerland

(Received 12 January 2014; accepted 4 March 2014; published online 17 March 2014)

We explore substoichiometric molybdenum trioxide ( $\text{MoO}_x$ ,  $x < 3$ ) as a dopant-free, hole-selective contact for silicon solar cells. Using an intrinsic hydrogenated amorphous silicon passivation layer between the oxide and the silicon absorber, we demonstrate a high open-circuit voltage of 711 mV and power conversion efficiency of 18.8%. Due to the wide band gap of  $\text{MoO}_x$ , we observe a substantial gain in photocurrent of  $1.9 \text{ mA/cm}^2$  in the ultraviolet and visible part of the solar spectrum, when compared to a p-type amorphous silicon emitter of a traditional silicon heterojunction cell. Our results emphasize the strong potential for oxides as carrier selective heterojunction partners to inorganic semiconductors. © 2014 AIP Publishing LLC. [<http://dx.doi.org/10.1063/1.4868880>]

Efficient carrier selective contacts and excellent surface passivation are key to solar cells with high power conversion efficiencies. Fundamentally, a solar cell consists of a light absorbing semiconductor bound on one side by a selective contact, which transmits holes and blocks electrons and on the other side by a complementary selective contact, which blocks holes and transmits electrons.<sup>1</sup> Under illumination, these selective contacts act like sinks for their respective carriers and establish a gradient in their corresponding chemical potentials which leads to diffusion current. Passivation of surface defects guarantees that photogenerated carriers are transmitted through the contacts before they recombine.

Silicon heterojunction solar cells, with demonstrated efficiencies of up to 24.7%,<sup>2</sup> represent a model photovoltaic system that employs a thin intrinsic hydrogenated amorphous silicon layer (a-Si:H) as surface passivation layer.<sup>3,4</sup> Carrier selectivity at the contacts is traditionally achieved by depositing a doped a-Si:H layer after passivation. With this approach record open-circuit voltages above 750 mV have been reported.<sup>3</sup>

However, with a band gap of only 1.7–1.8 eV, a strong absorption coefficient combined with a high defect density, a-Si:H, even when only a few nanometers thin, leads to significant parasitic absorption of light in the ultraviolet and visible region of the solar spectrum which does not contribute to photocurrent generation.<sup>5</sup> Eliminating current losses becomes even more critical in view of the recent trend to ever thinner wafers which enable higher open-circuit voltages.<sup>3,6</sup> Recent efforts to improve the cell current have focused on replacing a-Si:H with wider band gap a-SiO<sub>x</sub>:H or a-SiC<sub>x</sub>:H, but gains in photocurrent remained modest.<sup>7–10</sup>

Here, we demonstrate a radically different selective hole contact scheme for n-type silicon heterojunction solar cells based on thermally evaporated substoichiometric molybdenum

trioxide ( $\text{MoO}_x$ ,  $x < 3$ ) thin films.  $\text{MoO}_x$  has found wide-spread application as hole selective contact in organic electronics and photovoltaics.<sup>11–13</sup> We have recently shown that  $\text{MoO}_x$  can be considered to act like a high workfunction metal with a low density of states at the Fermi level originating from the tail of an oxygen-vacancy-derived defect band inside the band gap and have extended its application to crystalline silicon (c-Si) by demonstrating an unpassivated  $\text{MoO}_x$ /c-Si solar cell with 14.3% efficiency.<sup>14</sup> Here, by inserting an intrinsic a-Si:H passivation layer between the oxide contact and the silicon absorber,  $\text{MoO}_x$ /a-Si:H/c-Si, we obtain an efficiency of 18.8%. With a band gap of 3.3 eV,  $\text{MoO}_x$  contacts enable an impressive current gain of  $1.9 \text{ mA/cm}^2$  while maintaining the same open-circuit voltage ( $V_{oc}$ ) as compared to a standard silicon heterojunction solar cells fabricated using the same baseline process.

A schematic of the fabricated  $\text{MoO}_x$ /a-Si:H/c-Si solar cell is shown in Fig. 1(a) along with a false-colored scanning electron microscopy (SEM) cross section image in Fig. 1(b). Float-zone grown n-type Si(100) wafers with a resistivity of

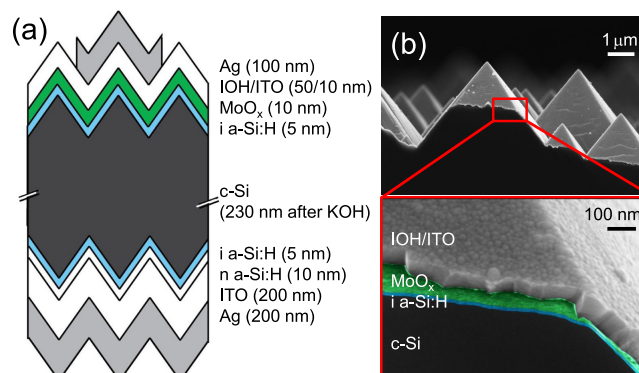


FIG. 1. (a) Schematics of the  $\text{MoO}_x$ /a-Si:H/c-Si heterojunction solar cell structure with (b) false-colored cross section imaged by scanning electron microscopy. Pyramids in (a) are not drawn to scale and are not necessarily commensurate on front and back side.

<sup>a)</sup>Author to whom correspondence should be addressed. Electronic mail: [ajavey@eecs.berkeley.edu](mailto:ajavey@eecs.berkeley.edu)

4  $\Omega\cdot\text{cm}$  were textured in potassium hydroxide (KOH); subsequently, cleaned via a RCA-type sequence (a standard wafer cleaning sequence developed by the Radio Corporation of America<sup>15</sup>) and dipped into hydrofluoric acid (HF) to remove the native oxide right before layer deposition. Wafer thickness after texturing is 230  $\mu\text{m}$ . Front- and backside of the wafer were passivated with intrinsic a-Si:H (5 nm) deposited by plasma-enhanced chemical vapor deposition (PE-CVD). Deposition details can be found in Ref. 16. On the frontside, a  $\text{MoO}_x$  layer (10 nm in thickness, unless otherwise stated) was thermally evaporated from a stoichiometric  $\text{MoO}_3$  powder source at a rate of 0.5  $\text{\AA}/\text{s}$  out of an alumina-coated tungsten boat at a base pressure of  $4 \times 10^{-6}$  Torr and coated with a sputtered hydrogenated indium oxide ( $\text{IOH} = \text{In}_2\text{O}_3:\text{H}$ ) transparent electrode (50 nm) capped with indium tin oxide ( $\text{ITO} = \text{In}_2\text{O}_3:\text{SnO}_2 = 90\%:10\%$ , 10 nm) through a  $2 \times 2 \text{ cm}^2$  shadow mask.<sup>17</sup> The thin ITO cap minimizes contact resistance between IOH and the Ag finger grid.<sup>18</sup> For comparison, we also fabricated a silicon heterojunction solar cell with standard boron-doped p-type a-Si:H emitter (10 nm) and ITO front electrode (70 nm), similar to the structures discussed in Refs. 16 and 18. The thicknesses for the front oxide electrodes differ for the case with  $\text{MoO}_x$  and p-type a-Si:H contacts in order to guarantee optimum antireflection conditions which are obtained for 70 nm total oxide thickness as the refractive indices of  $\text{MoO}_x$ , IOH, and ITO are all close to 2 in the visible regime. A phosphorus doped n-type a-Si:H layer (10 nm) was deposited on the backside to repel minority carriers from the sputtered ITO/Ag back contact (150 nm/200 nm)<sup>19</sup> with the help of the resulting back surface field. After screen printing of the Ag frontside finger grid using a low-temperature Ag paste, the cells were annealed at 200  $^\circ\text{C}$  on a belt furnace for 10 min.

In Figs. 2(a) and 2(b), we compare the energy band diagram for the cell with  $\text{MoO}_x$  hole contact to the one of the reference cell with p-type a-Si:H contact. The salient feature in both diagrams is the formation of an inversion layer in the c-Si absorber next to the  $\text{MoO}_x$  or p-type a-Si:H hole contact accompanied by a large barrier for electrons resulting from the band bending in c-Si and the conduction band offset between c-Si and a-Si:H. For both cases, holes, which reach the front surface of the cell, must cross the barrier resulting from the valence band offset between c-Si and a-Si:H before they can transit through the a-Si:H tail states or oxygen-vacancy-derived defect states in  $\text{MoO}_x$  into the degenerately

doped ITO front electrode and be extracted through the Ag fingers. Importantly, the width of this barrier is controlled by the  $\text{MoO}_x$  workfunction or p-type a-Si:H carrier concentration. While n-type  $\text{MoO}_x$  and p-type a-Si:H possess drastically different electronic properties, we can see from comparison of the band diagrams in Fig. 2 that they both provide a very similar situation for hole extraction in which defect states play an important role to ensure hole transport to the electrode.

We now discuss the impact of  $\text{MoO}_x$  on the optical performance and the photocurrent of the heterojunction cells. Fig. 3(a) compares the external quantum efficiency (EQE) of the fabricated cells measured without Ag grid. A dramatic increase in the blue and visible response is observed for the  $\text{MoO}_x$  compared to the standard p a-Si:H emitter translating into a substantial 1.9  $\text{mA}/\text{cm}^2$  gain in photocurrent at wavelengths below 700 nm. This enhancement is much stronger than the 0.4  $\text{mA}/\text{cm}^2$  gain observed by Seif *et al.*<sup>7</sup> when replacing the intrinsic a-Si:H passivation layer by intrinsic a-SiO<sub>x</sub>:H and is close to the maximum possible current enhancement of 2.1  $\text{mA}/\text{cm}^2$  assessed via modeling in Ref. 5.

Fig. 3(b) shows the absorbance ( $A = 100\% - R - T$ ) curves for  $\text{MoO}_x$  (10 nm), ITO (70 nm), and IOH (60 nm) determined by measuring reflectance ( $R$ ) and transmittance ( $T$ ) of witness layers co-deposited on glass with a photospectrometer. The data have been corrected for the absorbance of the glass slide at short wavelengths. The absorbance of a standard p-type doped a-Si:H emitter (10 nm) calculated from the extinction coefficient determined by spectroscopic ellipsometry is also shown. With a band gap of 3.3 eV, the absorption onset for  $\text{MoO}_x$  happens at much shorter wavelength ( $\sim 400 \text{ nm}$ ) than for p a-Si:H ( $\sim 600 \text{ nm}$ ). This explains the much improved EQE at short wavelengths. Note that the edge of the optical transmission window in the cell with  $\text{MoO}_x$  is determined by the indium oxide electrode whose absorption onset occurs at slightly lower wavelength. A small portion of the current gain can be ascribed to the steeper band edge of IOH compared to ITO, which increases the apparent gap slightly. In an earlier study comparing IOH and ITO for silicon heterojunction cells, no gain in EQE below 700 nm was observed when replacing ITO by IOH as the amorphous p-type emitter was the limiting factor for the blue response.<sup>18</sup> On the other hand, current gains of up to 1  $\text{mA}/\text{cm}^2$  in the blue have been demonstrated for thin-film silicon solar cells,<sup>21</sup> which use significantly more transparent nanocrystalline silicon oxide (nc-SiO<sub>x</sub>:H) emitters with

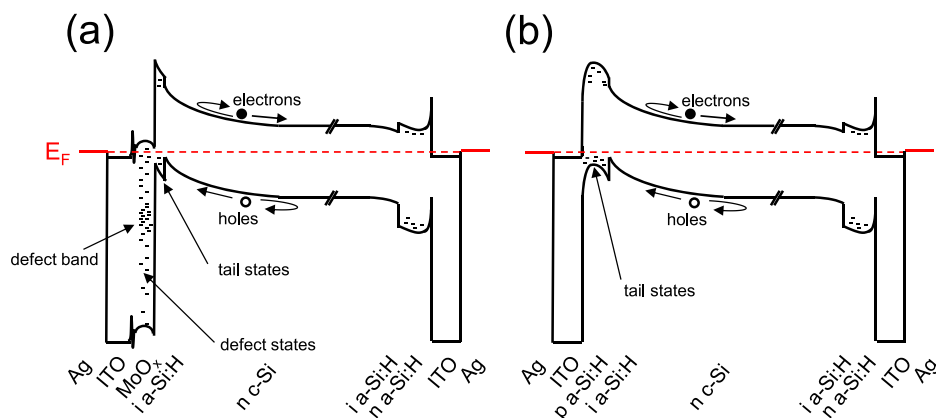


FIG. 2. Energy band diagrams for silicon solar cell with hole selective (a)  $\text{MoO}_x$  contact and (b) standard p-type a-Si:H emitter. Band offsets for a-Si:H with respect the c-Si were taken from Ref. 20, a workfunction of 5.7 eV was assumed for  $\text{MoO}_x$ ,<sup>14</sup> and a hole density of  $10^{19} \text{ cm}^{-3}$  for p-type a-Si:H was chosen.<sup>7</sup> Layer thicknesses along the horizontal axis are not to scale for readability. In particular, the depletion region in c-Si extends in reality about 1  $\mu\text{m}$  into the bulk.

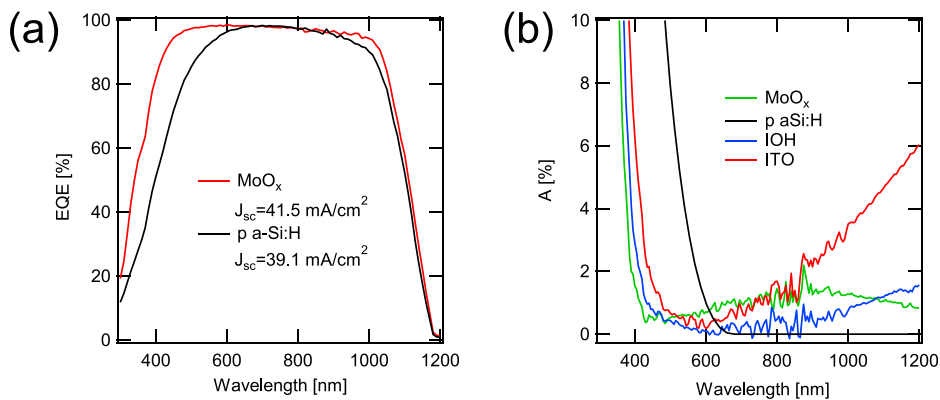


FIG. 3. (a) EQE comparison for a heterojunction cell with a MoO<sub>x</sub> selective hole contact and a standard p a-Si:H emitter. (b) Absorbance measurements for MoO<sub>x</sub>, p a-Si:H, IOH, and ITO.

indirect band gap.<sup>22,23</sup> However, these emitters are grown in harsh hydrogen-rich conditions with high plasma power which deteriorate the passivation of the silicon wafer.

The improvement in the red response for wavelengths longer than 600 nm in Fig. 3(a), accounting for  $0.5 \text{ mA/cm}^2$ , is due to the reduced free carrier absorption in IOH compared to ITO as seen in Fig. 3(b), due to the lower carrier concentration of IOH, permissible due to its high mobility ( $>100 \text{ cm}^2/\text{V}\cdot\text{s}$ ). This effect was investigated in Ref. 18. There, a  $1 \text{ mA/cm}^2$  gain in photocurrent was observed. Here, the gain is smaller ( $0.5 \text{ mA/cm}^2$ ), which is explained by the broad sub band gap absorption of MoO<sub>x</sub> observable in Fig. 3(b), which, in turn, is the signature of the oxygen-vacancy-derived defect band studied in detail in Ref. 14. Total photocurrents determined from the EQE by convolution with the global air mass 1.5 (AM1.5 g) spectrum are  $41.5 \text{ mA/cm}^2$  vs  $39.1 \text{ mA/cm}^2$ .

We now discuss how MoO<sub>x</sub> affects the passivation and electrical performance of the cells. Fig. 4(a) shows the

effective minority carrier lifetime of a-Si:H passivated silicon before and after MoO<sub>x</sub> evaporation as monitored using a quasi-steady state photoconductance measurement system with a flash lamp.<sup>24</sup> While the lifetime of unpassivated wafers after HF dip stabilizes typically at most at a few tens of  $\mu\text{s}$  in ambient air,<sup>25</sup> the lifetime rises to 2–3 ms after amorphous silicon deposition. At high minority carrier injection, the carrier lifetime in the wafer is limited by Auger recombination as shown by the black dashed line.<sup>26</sup> Importantly, thermal evaporation of MoO<sub>x</sub> affects the lifetime of the passivated wafer only minimally as can be seen from Fig. 4(a). In contrast, IOH sputtering degrades the carrier lifetime significantly and has been shown to be due to plasma luminescence and bombardment with high energy particles,<sup>27</sup> which are both absent during thermal evaporation. However, low-temperature annealing is known to eliminate almost completely the detrimental effects of sputtering on  $V_{oc}$ .<sup>27</sup> From the lifetime measurements, we can further determine the quasi-Fermi level

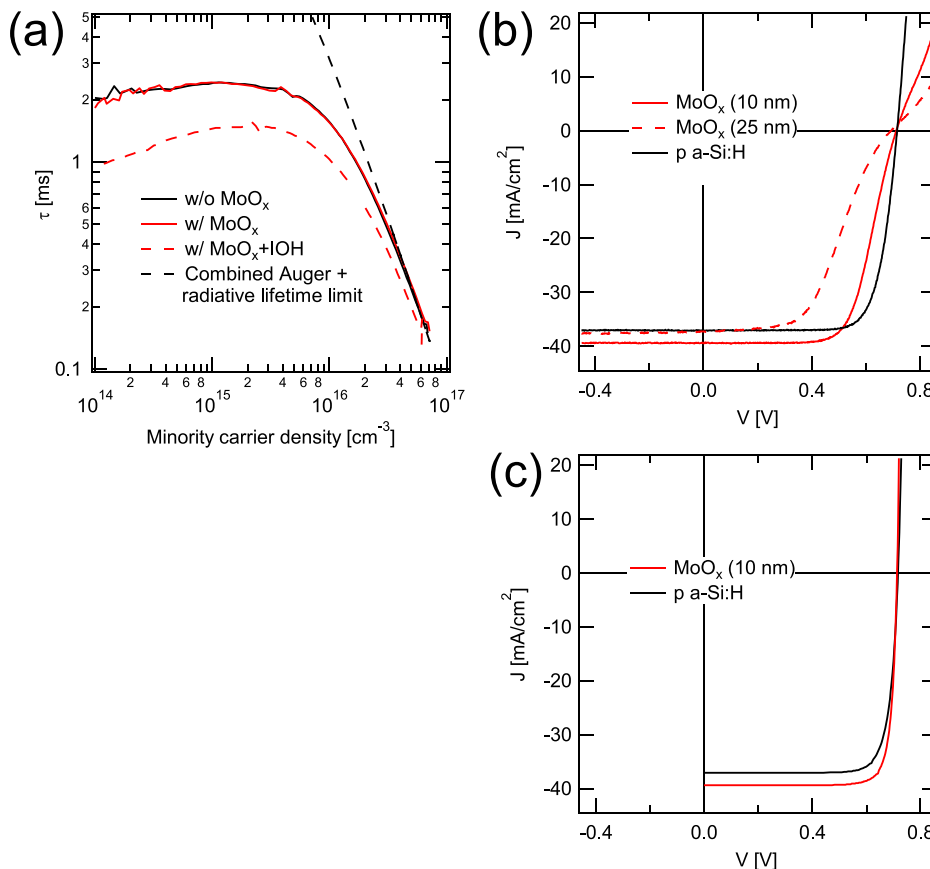


FIG. 4. (a) Minority carrier lifetime measurements before and after MoO<sub>x</sub> thermal evaporation and after IOH sputtering. (b)  $J$ - $V$  characteristics for a 10 nm and 25 nm MoO<sub>x</sub> selective hole contact and a standard p a-Si:H emitter. (c) Sun's  $V_{oc}$  measurements for the 10 nm MoO<sub>x</sub> and p a-Si:H cell.

TABLE I. Summary of cell performance parameters.

Hole contact	$V_{oc}$ (mV)	$J_{sc}$ (mA/cm <sup>2</sup> )	FF (%)	Efficiency (%)
MoO <sub>x</sub>	711	39.4	67.2	18.8
p a-Si:H	716	37.1	75.9	20.2

splitting (often called implied  $V_{oc}$ ), which is of the order of 725 mV at 1-sun and confirms the high quality of the passivation. It is important to note that even higher  $V_{oc}$  can be achieved with thinner wafers due to higher excess charge carrier densities per recombination volume.<sup>6,28,29</sup>

Fig. 4(b) shows current density-voltage ( $J$ - $V$ ) characteristics of the solar cells measured under standard test conditions (25 °C, 1000 W/m<sup>2</sup>, and AM1.5 g spectrum) from which we can extract the real  $V_{oc}$  of the cells. The MoO<sub>x</sub> cell approaches the  $V_{oc}$  of the standard reference cell closely with 711 mV vs 716 mV, respectively. This confirms that passivation is hardly affected by the MoO<sub>x</sub> deposition. The short-circuit current densities ( $J_{sc}$ ) of 39.4 mA/cm<sup>2</sup> for the MoO<sub>x</sub> cell vs. 37.1 mA/cm<sup>2</sup> for the reference cell are consistent with the currents determined from EQE taking into account 5% Ag grid shading. Cell performance parameters are summarized in Table I.

While  $V_{oc}$  and  $J_{sc}$  for the MoO<sub>x</sub> cells show comparable or improved performance, the  $J$ - $V$  curve for MoO<sub>x</sub> exhibits a slight “s-shape” indicating a problem with band alignment at the MoO<sub>x</sub>/a-Si:H/c-Si interfaces impeding the extraction of holes. This results in a markedly lower fill factor ( $FF$ ) of 67.2% for the MoO<sub>x</sub> based cell vs 75.9% for the standard cell and a power conversion efficiency of 18.8% vs 20.2%. The

s-shape becomes more pronounced when increasing the MoO<sub>x</sub> layer thickness to 25 nm (also shown in Fig. 4(b), the lower  $J_{sc}$  is due to the sub-optimal oxide thickness). The MoO<sub>x</sub> layer should, therefore, be kept as thin as possible, but thick enough to guarantee a continuous layer and an efficient barrier for electrons.

Fig. 4(c) shows Sun’s  $V_{oc}$  measurements, which track the  $V_{oc}$  of the cells as a function of illumination intensity. The resulting pseudo  $J$ - $V$  curves represent  $J$ - $V$  curves in the absence of series resistance losses as no current is flowing.<sup>32</sup> This shows the potential of the MoO<sub>x</sub> contact which achieves a pseudo efficiency of 23.9% vs 21.8% for the standard silicon heterojunction solar cell reference used here, primarily due to the higher current.

To better understand the origin of the s-shaped profile of the  $J$ - $V$  curve, we performed  $J$ - $V$  measurements as a function of temperature shown in Fig. 5(a). The temperature dependence for the reference cell is shown in Fig. 5(b). With increasing temperature the s-shape straightens out pointing towards a thermionic emission barrier, which the holes have to overcome.<sup>7</sup> The  $FF$  consequently improves slightly with increasing temperature as shown in Fig. 5(c). On the contrary, the  $FF$  of the standard cell reduces slightly with temperature.  $V_{oc}$  reduces in both cases by about  $-1.5$  mV/°C as shown in Fig. 5(d) and causes the efficiency to drop for both cells as shown in Fig. 5(e). Interestingly, upon linear extrapolation, the performance of the MoO<sub>x</sub> cell equalizes the performance of the standard cell at an operating temperature of 70 °C, which is not an unrealistic temperature for a photovoltaic module operated in the field.<sup>30</sup> An improved temperature coefficient has also been observed by Seif *et al.*,<sup>7</sup> who replaced the passivating i a-Si:H layer with a high band gap i

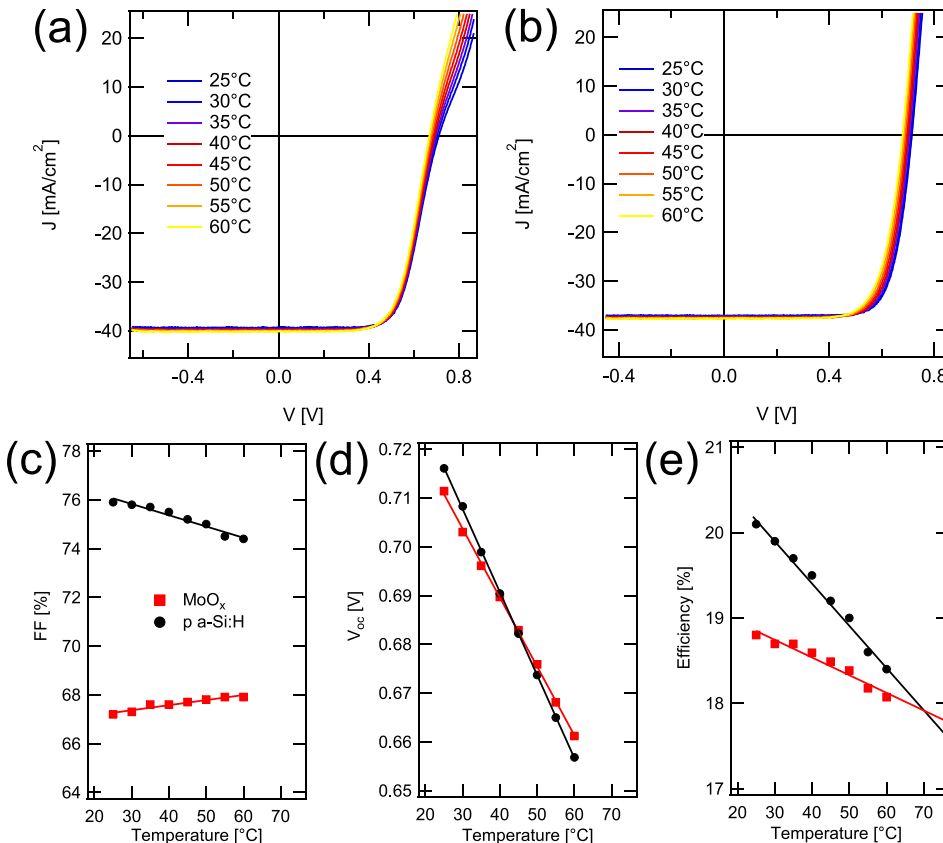


FIG. 5. Temperature evolution of  $J$ - $V$  curves for (a) MoO<sub>x</sub> contact and (b) p a-Si:H contact. Evolution of  $FF$  (c),  $V_{oc}$  (d), and cell efficiency (e) with temperature for both cells.



a-SiO<sub>x</sub>:H layer. However, if the s-shaped character of the *J*-*V* curve can be avoided using MoO<sub>x</sub> layers with higher work functions, for instance by eliminating carbon contaminants during processing<sup>14</sup> and/or chemical doping of MoO<sub>x</sub>, the temperature behavior of the resulting cell is expected to approach the performance characteristics of the standard cell.

Note that the low mobility of carriers in the MoO<sub>x</sub> defect band can add series resistance to the cell but cannot explain the s-shape (resistivity of MoO<sub>x</sub> ~ 200 Ω·cm (Ref. 31)). The temperature dependence of the *J*-*V* curve clearly indicates a misalignment of the MoO<sub>x</sub> Fermi level. In particular, the width of the hole barrier in the intrinsic a-Si:H layer in Fig. 2(a) reduces with increasing MoO<sub>x</sub> workfunction. The workfunction of MoO<sub>x</sub> is known to be sensitive to adventitious carbon and water adsorption upon air exposure, but can reach up to 6.6 eV or higher when ultra-clean.<sup>14</sup> Thus, besides using thinner MoO<sub>x</sub>, capping of MoO<sub>x</sub> by IOH/ITO in vacuum could be a possible solution to improve band alignment, reduce the hole barrier and improve *FF*. A thinner MoO<sub>x</sub> would also permit a thicker IOH/ITO layer, while maintaining a total oxide thickness of 70 nm for optimum antireflection, reducing series resistance, and improving *FF* further.

In conclusion, we have introduced MoO<sub>x</sub> as a hole selective contact for passivated silicon heterojunction solar cells delivering a respectable efficiency of 18.8% for such an exploratory approach. Improved optical transparency improves the total photocurrent by 2.4 mA/cm<sup>2</sup>. Open-circuit voltage is as high as for the state-of-the-art cells. Future work needs to focus on improving the fill factor. More generally, our results demonstrate that oxide-based selective hole contacts with workfunctions exceeding those of elemental metals,<sup>33</sup> present an important opportunity not only for traditional IV, III–V, and II–VI semiconductors but also for emerging semiconducting nanomaterials.

MoO<sub>x</sub> processing, characterization, and device integration were funded by the Director, Office of Science, Office of Basic Energy Sciences, and Division of Materials Sciences and Engineering of the U.S. Department of Energy under Contract No. De-Ac02-05Ch11231 and the Electronic Materials (E-Mat) program. Photovoltaic device fabrication and characterization were funded by the Bay Area Photovoltaics Consortium (BAPVC) and the Swiss Federal Energy Office. We thank L. Barraud, J. Seif, and B. Demareux for stimulating discussions and technical support and N. Badel for screen printing. C. Battaglia acknowledges support from the Zeno Karl Schindler Foundation.

<sup>1</sup>P. Würfel, *Physics of Solar Cells: From Principles to New Concepts* (Wiley, Weinheim, Germany, 2005).

<sup>2</sup>M. A. Green, K. Emery, Y. Hishikawa, W. Warta, and E. D. Dunlop, *Prog. Photovoltaics: Res. Appl.* **21**, 1 (2013).

- <sup>3</sup>M. Taguchi, A. Yano, S. Tohoda, K. Matsuyama, Y. Nakamura, T. Nishiwaki, K. Fujita, and E. Maruyama, *IEEE J. Photovoltaics* **4**, 96 (2014).
- <sup>4</sup>S. De Wolf, A. Descoedres, Z. C. Holman, and C. Ballif, *Green* **2**, 7–24 (2012).
- <sup>5</sup>Z. C. Holman, A. Descoedres, L. Barraud, F. Z. Fernandez, J. P. Seif, S. De Wolf, and C. Ballif, *IEEE J. Photovoltaics* **2**, 7–15 (2012).
- <sup>6</sup>S. Y. Herasimenka, W. J. Dauksher, and S. G. Bowden, *Appl. Phys. Lett.* **103**, 053511 (2013).
- <sup>7</sup>J. P. Seif, A. Descoedres, M. Filipic, F. Smole, M. Topic, Z. C. Holman, S. De Wolf, and C. Ballif, *J. Appl. Phys.* **115**, 024502 (2014).
- <sup>8</sup>H. Fujiwara, T. Kaneko, and M. Kondo, *Appl. Phys. Lett.* **91**, 133508 (2007).
- <sup>9</sup>D. Pysch, M. Bivour, M. Hermle, and S. W. Glunz, *Thin Solid Films* **519**, 2550–2554 (2011).
- <sup>10</sup>T. Mueller, S. Schwertheim, M. Scherff, and W. R. Fahrner, *Appl. Phys. Lett.* **92**, 033504 (2008).
- <sup>11</sup>J. Meyer, S. Hamwi, M. Kröger, W. Kowalsky, T. Riedl, and A. Kahn, *Adv. Mater.* **24**, 5408–5427 (2012).
- <sup>12</sup>M. T. Greiner, M. G. Helander, W.-M. Tang, Z.-B. Wang, J. Qiu, and Z.-H. Lu, *Nature Mater.* **11**, 76 (2012).
- <sup>13</sup>S. Tokito, K. Noda, and Y. Taga, *J. Phys. D: Appl. Phys.* **29**, 2750–2753 (1996).
- <sup>14</sup>C. Battaglia, X. Yin, M. Zheng, I. D. Sharp, T. Chen, S. McDonnell, A. Azcatl, C. Carraro, R. Maboudian, R. M. Wallace, and A. Javey, *Nano Lett.* **14**, 967–971 (2014).
- <sup>15</sup>W. Kern and D. A. Puotinen, *RCA Rev.* **31**, 187 (1970).
- <sup>16</sup>A. Descoedres, L. Barraud, S. De Wolf, B. Strahm, D. Lachenal, C. Buerin, Z. C. Holman, F. Zicarelli, B. Demareux, J. Seif, J. Holovsky, and C. Ballif, *Appl. Phys. Lett.* **99**, 123506 (2011).
- <sup>17</sup>C. Battaglia, L. Erni, M. Boccard, L. Barraud, J. Escarré, K. Söderström, G. Bugnon, A. Billet, L. Ding, M. Despeisse, F.-J. Haug, S. De Wolf, and C. Ballif, *J. Appl. Phys.* **109**, 114501 (2011).
- <sup>18</sup>L. Barraud, Z. C. Holman, N. Badel, P. Reiss, A. Descoedres, C. Battaglia, S. De Wolf, and C. Ballif, *Sol. Energy Mater. Sol. Cells* **115**, 151–156 (2013).
- <sup>19</sup>Z. C. Holman, M. Filipic, A. Descoedres, S. De Wolf, F. Smole, M. Topic, and C. Ballif, *J. Appl. Phys.* **113**, 013107 (2013).
- <sup>20</sup>R. Varache, J. P. Kleider, W. Favre, and L. Korte, *J. Appl. Phys.* **112**, 123717 (2012).
- <sup>21</sup>C. Battaglia, J. Escarré, K. Söderström, L. Erni, L. Ding, G. Bugnon, A. Billet, M. Boccard, L. Barraud, S. De Wolf, F.-J. Haug, M. Despeisse, and C. Ballif, *Nano Lett.* **11**, 661 (2011).
- <sup>22</sup>M. Despeisse, C. Battaglia, M. Boccard, G. Bugnon, M. Charrière, P. Cuony, S. Hänni, L. Löfgren, F. Meillaud, G. Parascandolo, T. Söderström, and C. Ballif, *Phys. Status Solidi A* **208**, 1863–1868 (2011).
- <sup>23</sup>C. Battaglia, C.-M. Hsu, K. Söderström, J. Escarré, F.-J. Haug, M. Charrière, M. Boccard, M. Despeisse, D. T. L. Alexander, M. Cantoni, Y. Cui, and C. Ballif, *ACS Nano* **6**, 2790 (2012).
- <sup>24</sup>R. A. Sinton and A. Cuevas, *Appl. Phys. Lett.* **69**, 2510–2512 (1996).
- <sup>25</sup>S. Olibert, Ph.D. thesis, Université de Neuchâtel, Neuchâtel, 2008.
- <sup>26</sup>A. Richter, S. W. Glunz, F. Werner, J. Schmidt, and A. Cuevas, *Phys. Rev. B* **86**, 165202 (2012).
- <sup>27</sup>B. Demareux, S. De Wolf, A. Descoedres, Z. C. Holman, and C. Ballif, *Appl. Phys. Lett.* **101**, 171604 (2012).
- <sup>28</sup>E. Yablonoitch, D. L. Allara, C. C. Chang, T. Gmitter, and T. B. Bright, *Phys. Rev. Lett.* **57**, 249 (1986).
- <sup>29</sup>T. Tiedje, E. Yablonoitch, G. D. Cody, and B. G. Brooks, *IEEE Trans. Electron Devices* **31**, 711 (1984).
- <sup>30</sup>M. C. Alonso García and J. L. Balenzategui, *Renewable Energy* **29**, 1997 (2004).
- <sup>31</sup>S. Chuang, C. Battaglia, A. Azcatl, S. McDonnell, J. S. Kang, X. Yin, M. Tosun, R. Kapadia, H. Fang, R. M. Wallace, and A. Javey, *Nano Lett.* **14**, 1337–1342 (2014).
- <sup>32</sup>M. J. Kerr and A. Cuevas, *Sol. Energy* **76**, 263–267 (2004).
- <sup>33</sup>H. B. Michaelson, *J. Appl. Phys.* **48**, 4729 (1977).